metals

Article

Development and Characterization of CoCrMo/xCu Composites Fabricated by Powder Metallurgy

Luis Olmos [1,*], Armando Michel Garcia-Carrillo [2], Jose Lemus-Ruiz [2], Omar Jiménez [3], Dante Arteaga [4], Julio Cesar Villalobos-Brito [5] and Melina Velasco-Plascencia [6]

[1] Instituto de Investigaciones en Ciencias de la Tierra, Universidad Michoacana de San Nicolás de Hidalgo, Fco. J. Mujica S/N CU, Morelia C.P. 58060, Mexico
[2] Instituto de Investigación en Metalurgia y Materiales, Universidad Michoacana de San Nicolás de Hidalgo, Fco. J. Mujica S/N CU, Morelia C.P. 58060, Mexico; armando.michel.garcia@umich.mx (A.M.G.-C.); jlruiz@umich.mx (J.L.-R.)
[3] Departamento de Ingeniería de Proyectos, Universidad de Guadalajara, José Guadalupe Zuno # 48, Los Belenes, Zapopan C.P. 45100, Mexico; omar.aleman@academicos.udg.mx
[4] Centro de Geociencias, Universidad Nacional Autónoma de México, Blvd. Juriquilla No. 3001, Querétaro C.P. 76230, Mexico; darteaga@geociencias.unam.mx
[5] Departamento de Metal Mecánica Posgrado en Metalurgia/Instituto Tecnológico de Morelia, Av. Tecnológico 1500, Lomas de Santiaguito, Morelia C.P. 58120, Mexico; julio.vb@morelia.tecnm.mx
[6] Departamento de Ingeniería en Materiales, Tecnológico Nacional de México/Instituto Tecnológico de Morelia, Avenida Tecnológico No. 1500, Lomas de Santiaguito, Morelia C.P. 58120, Mexico; melina.vp@morelia.tecnm.mx
* Correspondence: luis.olmos@umich.mx

Abstract

This study aims to develop CoCrMo/xCu composites through liquid phase sintering. The primary focus is on investigating how the addition of copper influences sintering kinetics, microstructure, and mechanical properties. The copper volume fraction ranged from 10 to 25 wt.% relative to CoCrMo. Sintering was conducted at 1150 °C under an argon atmosphere. Characterization methods included scanning electron microscopy, computed microtomography, and X-ray diffraction analysis. It was observed that molten copper, which forms upon reaching its melting temperature, can fill the interparticle spaces left by CoCrMo particles in the green compacts. During sintering, densification is further enhanced by the dissolution of CoCrMo, resulting in the formation of intermetallic phases enriched in Cr and Mo, as well as a ternary Co-Cr-Cu compound. Both densification and intermetallic formation contribute to increased microhardness as Cu content rises. It is concluded that the CoCrMo/25Cu composite exhibits the best mechanical and corrosion properties because its densification was improved by the Cu liquid.

Keywords: sintering kinetics; microstructure; computed microtomography; biomaterials; corrosion

Check for updates

Academic Editor: Jürgen Eckert

Received: 14 April 2026
Revised: 12 May 2026
Accepted: 21 May 2026
Published: 23 May 2026

Copyright: © 2026 by the authors. Licensee MDPI, Basel, Switzerland. This article is an open access article distributed under the terms and conditions of the Creative Commons Attribution (CC BY) license.

1. Introduction

CoCrMo-based alloys are the focus of extensive research because of their biocompatibility, corrosion resistance, and high hardness. These characteristics together enhance their wear resistance, making them one of the most commonly used materials for bone implant applications [1–4]. Many efforts to increase the mechanical and anticorrosion properties of CoCrMo alloys have been tried, with different kinds of reinforcing elements such as Si [5], Ni [6], Zn [7], Ti [8], TiO_2 [9], Al_2O_3 [10], calcium phosphate [11], and hydroxyapatite [12], to name a few. Conversely, copper (Cu) is an essential trace element for organisms that

cannot be produced or synthesized by the body, so it must be acquired through food [13]. Copper (Cu) is widely employed as a contact material owing to its outstanding thermal and electrical conductivity. While it has many benefits, it also has limitations regarding mechanical strength, physical durability, wear resistance, and corrosion resistance, which restrict its applications. Copper is used in biomaterials due to its antimicrobial properties, its ability to promote healing, and its compatibility with the human body [14]. This makes it a versatile material for various medical and biomedical applications, such as antibacterial agents, bone cement, hydrogels, and scaffolds for bone tissue [15]. More recently, it has also been utilized in the development of nanomaterials for cancer treatment [16,17].

Recent research emphasizes that powder metallurgy (PM) greatly improves the mechanical properties of copper-based metal matrix composites (MMCs) by using hybrid reinforcements. Hybrid reinforcements, which consist of two or more types of particles, are more effective than those that use only one type. Studies focus on optimizing mechanical, physical, and abrasion resistance properties by adjusting the proportions, sizes, and distributions of particles in the matrix. Increasing the proportion of particles, reducing their size, and achieving better dispersion enhance mechanical properties, hardness, and abrasion resistance, but reduce ductility and the coefficient of friction. An excessive number of particles can weaken the composite [18]. In liquid phase sintering, two scenarios arise depending on how the liquid phase forms: spontaneously, or through a eutectic reaction. The primary goal of liquid-phase sintering is not densification, but rather the rapid formation of interparticle solid bonds and the improved homogenization of alloying elements within the microstructure [19]. Time controls the amount and movement of the liquid phase. If the sintering time is too long, it can lead to excessive gas production, which reduces the liquid phase's viscosity and promotes pore connection, resulting in increased pores, thinner pore walls, and reduced compressive strength [20]. The antibacterial activity of various titanium (Ti) systems containing copper (Cu) additions has been studied [21]. For instance, the well-studied Ti64/Cu system exhibits the release of stable and continuous Cu^{2+} ions [22], which contributes to its antibacterial effectiveness [23]. Similar research has also been conducted on different kinds of steels. Martensitic steels have been doped with copper [24] and subjected to terminal treatment processes to enhance their corrosion resistance [25]. Stainless steels, such as 316L, 317L, and 304L, have demonstrated excellent biocompatibility in vitro and in vivo, proving to be safe and non-toxic for bone cells [26,27]. It has been reported that different heat treatments influence wear resistance, corrosion, and tribocorrosion in CoCrMo alloys with copper additions less than 4 wt.% [28]. It was found that corrosion resistance increased, but the incorporation of copper damaged the tribological properties. Additionally, antibacterial properties remained unchanged with heat treatments; these treatments facilitated adjustments in the microstructure by promoting carbide formation, which in turn enhanced mechanical properties, such as hardness. The phase transformation between the austenitic (FCC-γ) and martensitic (HCP-ε) structures, as well as the final microstructure of the CoCrMo/xCu system, has been previously investigated. The results demonstrate that increasing copper (Cu) content promotes the formation of the fcc phase, indicating that Cu acts as a stabilizing agent for the austenitic phase [14]. A related study conducted by Azun et al. [29] investigated a copper matrix reinforced with 0–15 wt.% Co and CrC, which was fabricated using powder metallurgy. The results showed that as the reinforcement content increased, the composites experienced a reduction in relative density. However, they displayed enhancements in hardness and abrasion resistance when compared to unreinforced specimens. The optimal properties, including enhanced tensile strength, were achieved at 10 wt.% reinforcement.

CoCrMo powders are usually sintered at temperatures ranging from 1200 to 1400 °C. As the temperature rises, the density increases [1–4]. Reducing the sintering temperature

saves energy and reduces operating costs while minimizing defects such as excessive grain growth, porosity, or deformation. It also facilitates greater control over final material properties, such as density, microstructure, and mechanical characteristics, improving product quality. Lower-melting-point materials sinter first in sintering and can form a liquid phase that acts as a binder (liquid-phase-assisted sintering) or redistributes around the higher-melting-point material, promoting a more homogeneous mixture. In cases where the lower-melting-point-material densifies more rapidly, if the shrinkage is not uniform, this can cause internal stresses in the mixture and, in some cases, micro-cracks. The density of copper and CoCrMo alloy is very similar, 8.94 and 8.29, respectively. The effect is therefore expected to be minor. The purpose of this study is to analyze the impact of copper inclusion in the commercial alloy CoCrMo and to develop a low-temperature composite through powder metallurgy and liquid-phase sintering. Kinetic analysis was developed using dilatometry tests, and metallographic characterization by microtomography, scanning electron microscopy (SEM), and X-ray diffraction (XRD). Finally, hardness tests were performed to determine the mechanical properties of the fabricated composites.

2. Materials and Methods

The study utilized commercial CoCrMo and Cu powders supplied by Sigma-Aldrich (St. Louis, MO, USA), which were spherical and had particle sizes less than 25 µm. Four types of specimens were fabricated, all of which were mixtures of CoCrMo and Cu powders with varying Cu quantities (10, 15, 20, and 25 wt.%). The CoCrMo/xCu powders were mixed in a turbula for 30 min in dry conditions. Following mixing, the powder was uniaxially pressed at 450 MPa in a 6 mm stainless steel die to form 3 mm tall cylindrical compacts with green densities close to 70%. The compacts underwent a thorough sintering process at a heating rate of 15 °C min^{-1} to 1150 °C, with a holding time of 1 h, and were finally cooled at 25 °C min^{-1} in a high-purity argon environment, using a L75 vertical dilatometer (Selb, Germany). The sintered sample was cut, and the cross-section was polished to achieve a mirror finish. Microtomography analysis was performed using the Versa-510 Zeiss nanotomography system (Zeiss, Jena, Germany) with an energy of 60 kV, capturing 1600 radiographies in one hour, and then analyzed with Avizo® software version 2019. Microstructural analysis was conducted utilizing a JEOL JSM-7600F field-emission scanning electron microscope (FE-SEM) (Tokyo, Japan). X-ray diffraction analysis (XRD) was performed using a D8 Bruker diffractometer (Bremen, Germany). The XRD patterns were acquired with K-alpha copper radiation at an energy setting of 30 kV and a current of 30 mA. The measurements utilized a step size of 0.2° and a time increment of 1 s, covering a 2θ range from 30° to 90°. The electrochemical evaluation was performed in a three-electrode cell, using an Ag/AgCl electrode as the reference, a platinum mesh as the counter electrode, and samples of 10Cu, 15Cu, 20Cu, and 25Cu as working electrodes. The samples were evaluated in Hank's solution and immersed for 50 min at open circuit potential. After that, a potentiodynamic test was conducted from −0.5 to 1 V vs. Ag/AgCl (sat) at a scan rate of 1 mV/s to evaluate corrosion behavior. Electrochemical impedance spectroscopy (EIS) was also performed over a frequency range of 100 kHz to 10 mHz with a 10 mV amplitude to evaluate corrosion mechanisms and polarization resistance. Finally, Vickers microhardness (HV) measurements were carried out using a Mitutoyo microhardness tester MVK-HVL (Kawasaki, Japan) with a 100 g load for 15 s, averaging 25 indentations in a 5 × 5 matrix. Indentations were made across the entire surface, with a 0.5 mm separation between measurements.

3. Results and Discussion

3.1. Sintering Analysis

Figure 1a illustrates the axial deformation as a function of time and temperature throughout the thermal cycle, with a maximum temperature of 1150 °C for the sintered CoCrMo samples with varying amounts of Cu. At the beginning of the process, the material is thermally expanded. The shrinkage is more significant as a function of the increase in temperature and the increase in Cu content in the system. This indicates that a higher amount of liquid generates a better rearrangement of particles in the compact, increasing the composite's densification.

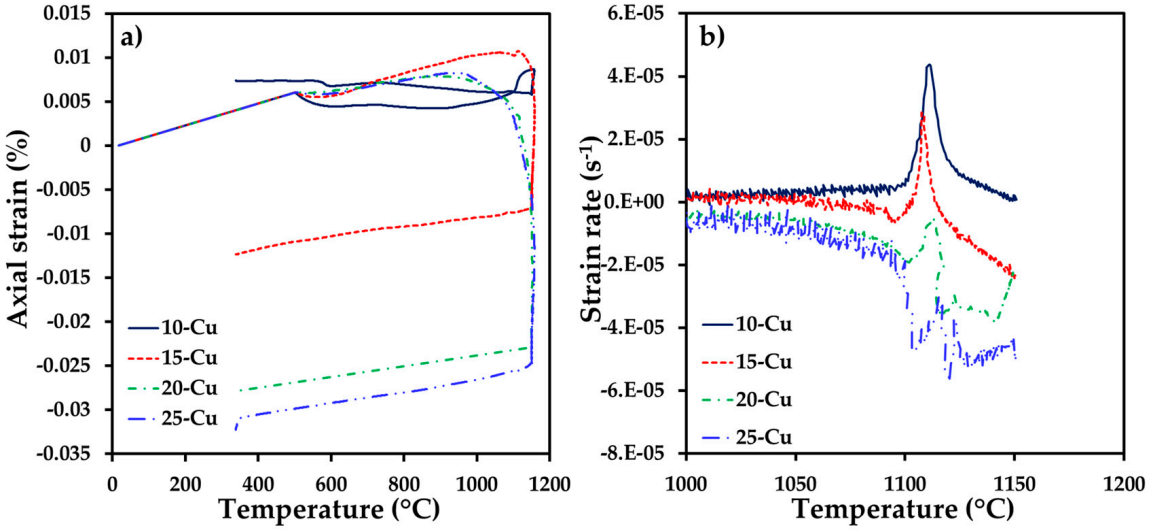


Figure 1. Axial deformation of CoCrMo/xCu composites during the whole sintering cycle (**a**), and the strain rate from 1000 to 1150 °C (**b**), as a function of the temperature.

Figure 1b shows the strain rate of composites with different amounts of Cu as a function of temperature in the range near the melting point of Cu. It was found that the strain rate is close to 0 for Cu contents less than 10 wt.%, indicating lower densification. On the contrary, samples with higher Cu contents exhibit higher densification, until 1096 °C is reached, suggesting that the liquid can spread among the interparticle porosity. At that point, there is an abrupt change in the strain rate, indicating that the Cu particles transition from a solid to a liquid state. For the case of lower amounts of 15% Cu, the observed peak is positive, indicating a dilation of the sample, which is logical since the volume of the liquid occupies a larger space than the solid. Immediately after reaching the maximum peak, a negative strain rate is observed, indicating that the liquid spreads between the pores left by the CoCrMo particles, resulting in compact densification. The strain rate shows a more negative value as the amount of Cu increases, suggesting that more liquid allows better densification and agrees with the total deformation of the compact measured in Figure 1a. This behavior suggests that densification takes place by the filling of interparticle pores, which are interconnected with each other and allow the flow of liquid Cu. This is mainly carried out by the capillary pressure exerted by the liquid over the solid surface of CoCrMo particles, as suggested by the densification model proposed by Lui et al. [30,31]. The shrinkage obtained during the previous heating stage to reach the sintering plateau is negligible when the liquid fraction is less than 15%, as shown in Figure 1a. On the other hand, the shrinkage reached during heating is larger for samples with higher liquid content, around 18% of the total shrinkage. This suggests a good wettability between the Cu liquid and the CoCrMo solid surfaces; however, the densification of samples does not reach an equilibrium before the sintering plateau.

Figure 2a shows the axial strain and the strain rate during the sintering plateau as a function of time, where it is observed that samples with Cu lower than 20 wt.% reached a more or less constant value at around 1500 s. This suggests that the capillary pressure reached a similar value, indicating that further shrinkage cannot be possible by filling the pores. The sample with a 25 wt.% of Cu shows a different trend; although the strain rate shows a constant value, the axial deformation does not show a constant value.

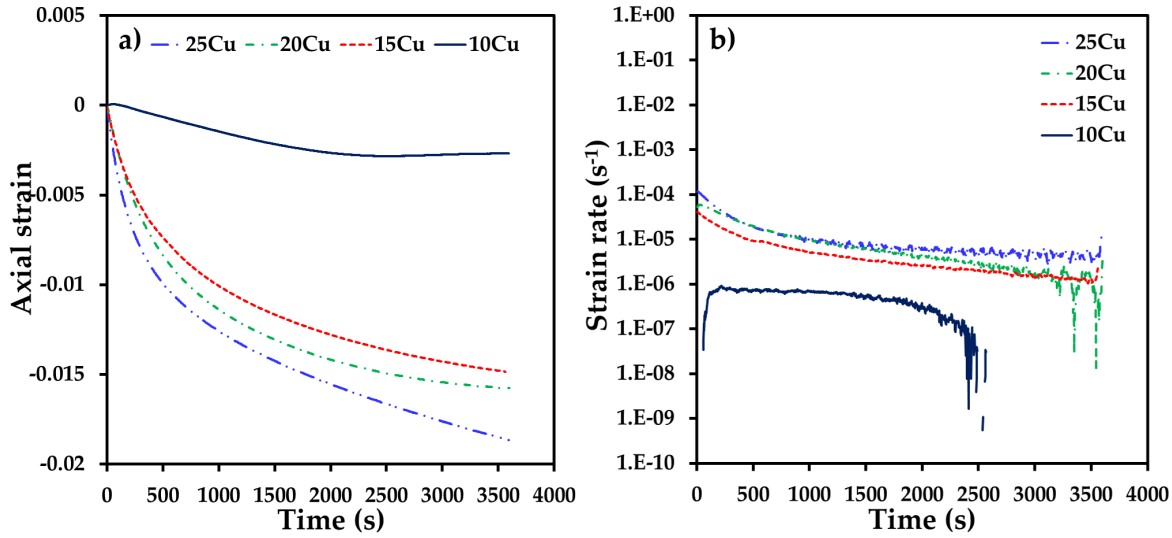


Figure 2. Axial strain (**a**) and strain rate (**b**) as a function of temperature during isothermal sintering at 1150 °C of the CoCrMo/xCu composites.

After the capillary forces reach a constant value, the strain rate diminishes; nevertheless, it is not null for all samples. This suggests that further densification is achieved during the sintering plateau. Thus, it is assumed that densification is driven by the dissolution of CoCrMo particles and their rearrangement, as previously suggested elsewhere [19]. Although Cu and Co are practically immiscible, Cao et al. [32] reported as a result of thermodynamic analysis that from 1140 °C, small quantities of Co can be dissolved by the Cu matrix, forming a phase rich in Cu with up to 13 at.% of Co. Those results were validated by experimental analysis during solidification of Co-Cu alloys by Munitz et al. [33,34]. This suggests that despite Cu and Co being immiscible in the liquid phase, as suggested by prior work [35,36], Cu liquid can dissolve the surface of the CoCrMo particles and then redistribute the matter by solution precipitation, which helps to enhance densification and strengthen the necks developed during solid-state sintering. This assumption is confirmed by the deformation observed on the CoCrMo particles, as shown in Figure 3.

In order to estimate the porosity of samples, the density was determined by weighing and measuring the volume as follows:

$$\rho = \frac{m}{V}, \tag{1}$$

where ρ is the density, m is the mass, and V is the volume of the cylindrical compact. The relative density is defined as the weight density of the compact divided by the theoretical density of the fully dense CoCrMo/xCu composite at room temperature, which was calculated by using the mixture law:

$$\rho_t = \rho_1 f_1 + \rho_2 f_2, \tag{2}$$

where ρ_i and f_i are the theoretical density and the volume fraction of component i. Therefore, the relative density can be estimated during the complete sintering cycle as follows:

$$D = \frac{\rho}{\rho_t}. \quad (3)$$

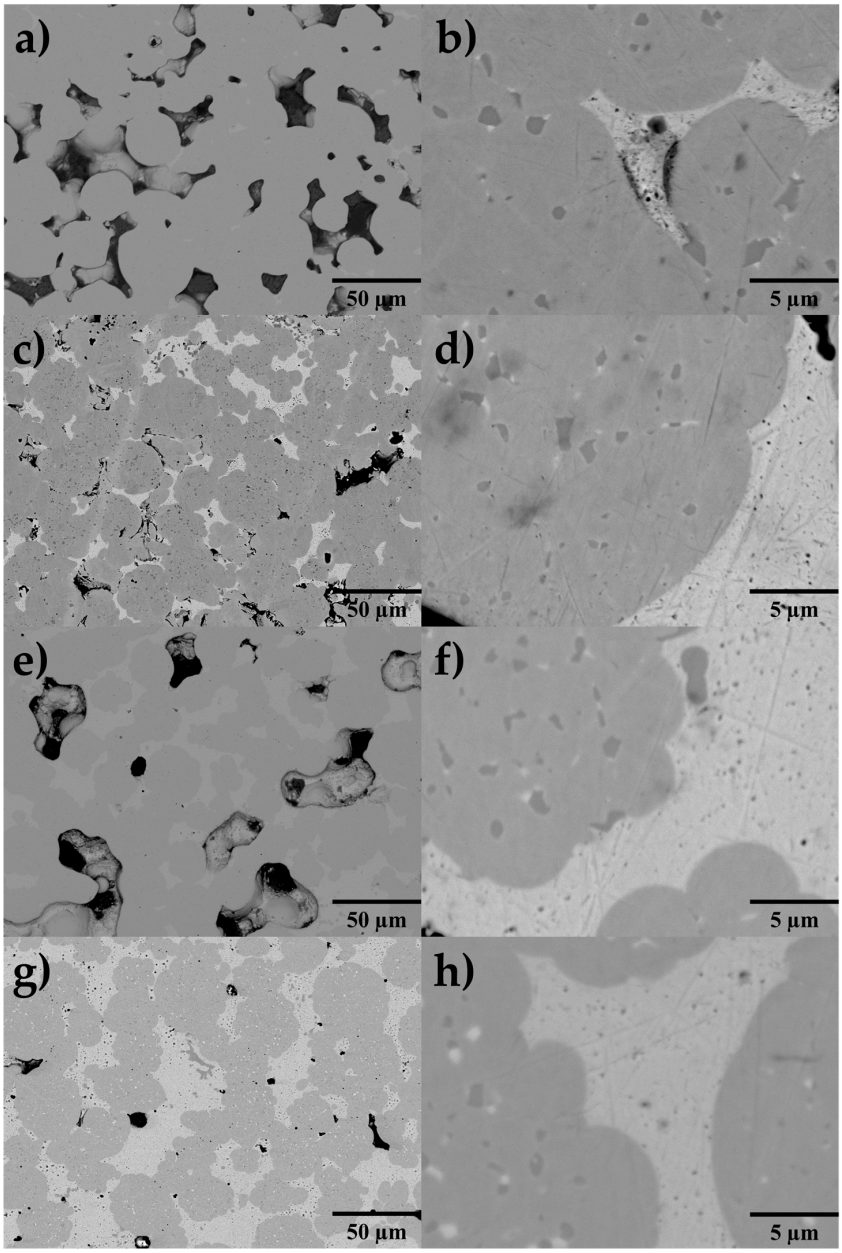


Figure 3. Microstructure of sintered CoCrMo/Cu composites at 1150 °C with 10 wt.% Cu (**a**,**b**), 15 wt.% Cu (**c**,**d**), 20 wt.% Cu (**e**,**f**), and 25 wt.% Cu (**g**,**h**), imaged using backscattered electrons.

The relative density indicates the volume occupied by the solid in the samples; therefore, the pore volume fraction can be deducted by the difference in the unity and the relative density (1 − D). Samples were measured before and after the sintering, and the values of the relative densities were named D_g and D_s, respectively, and listed in Table 1. As expected, the addition of Cu increases the green density because it undergoes a larger plastic deformation during powder compaction. The relative density of samples ranged from 0.81 to 0.95, increasing as the Cu addition increased. This is consistent with the axial deformation reached during sintering. The densification reached after sintering is estimated

as $(D_s - D_g)/D_g$, which indicates the elimination of pores during liquid sintering. This confirms that densification is mainly due to pore filling, in which the quantity of liquid plays a crucial role. The densification reached when 25 wt.% of Cu is added is 35 times larger in comparison to the sample with 10 wt.%.

Table 1. Relative densities, densification, and pore volume fraction of CoCrMo/xCu composites.

Sample	D_g	D_s	$(D_s - D_g)/D_g$	Pore Volume Fraction
CoCrMo-10Cu	0.8091	0.8113	0.0026	0.1886
CoCrMo-15Cu	0.8299	0.8574	0.0330	0.1425
CoCrMo-20Cu	0.8652	0.9186	0.0617	0.0813
CoCrMo-25Cu	0.8763	0.9560	0.0908	0.0439

3.2. Microstructural Characterization

Micrographs of the fabricated materials at different magnifications were obtained using backscattered electrons. Two main phases are observed at lower magnifications: the CoCrMo matrix and Cu. The microstructure also shows the residual porosity left after sintering. It is observed that more pores remain as the wt.% of Cu diminishes, which is logical because the quantity of liquid is not enough to fill the whole interparticle porosity. In the 10 wt.% Cu specimen, the spherical CoCrMo particles can be easily distinguished, as well as the necks between particles obtained during the solid-state sintering among the CoCrMo particles. As the Cu content increases, the necks begin to grow until they disappear, forming new particles, and these begin to lose their sphericity at the CoCrMo/Cu interface, as observed in the 25 Cu specimens (see Figure 3d,h).

At lower concentrations of Cu (10 and 15%), it is mainly isolated from the CoCrMo particles, as shown in Figure 3a,b,e,f. However, as the amount of Cu in the system increases, it fills the empty spaces between the CoCrMo particles, allowing for a more significant densification of the manufactured part, as shown in Figure 3c,d,g,h. This confirms the results obtained from dilatometry. Additionally, Figure 3 confirms that the Cu liquid can effectively surround the surface of the CoCrMo particles, indicating good wettability of the system.

At higher magnifications inside of the CoCrMo particles, two different intermetallic phases were observed to precipitate, that are qualitatively identified by the differences in contrast in the micrographs in Figure 3. To confirm their composition, elemental mapping and EDS analysis were performed (see Figure 4), the lighter one being a Mo-rich intermetallic and the darker one an intermetallic with high Cr content. In addition, a phenomenon of Cu diffusion towards the surface of the CoCrMo particles was observed. The elemental mappings and the chemical composition obtained by EDS are reported in Figure 4 and Table 2. The phases involved in this process include CoCr, which results from the decomposition of CoCrMo. Additionally, two new phases begin to precipitate within the CoCrMo matrix: $Co_{0.8}Cr_{0.2}$, which has a higher chromium content, and pure Mo. A more detailed discussion of these phases can be found in the X-ray section.

Subsequently, a line scan and EDS analysis were performed at the interface (Figure 5a) of the main CoCrMo and Cu phases. The size of the Cr and Mo intermetallic compounds was quantified, with Cr being smaller and more dispersed than those of Mo due to the smaller amount of Cr present in the system. The amount of Cu that diffuses in the CoCrMo matrix and the distance that Cu manages to penetrate into the CoCrMo matrix, which is 0.8 microns, was also quantified. EDS analysis conducted in a zone with a diameter lower than 1 micron corroborates the variation in Cu found by line scan (Figure 5b,c), which ranges from 35 to 48%. Also, notice that the Mo in this zone is not detected. In this zone, it is believed that a dissolution of the CoCrMo particles is achieved by the Cu liquid, which

helps with the final densification of the samples. The EDS analysis indicates that not only the Co is dissolved by the Cu, which leads to a phase composed of Co, Cu and Cr in a minor quantity. However, the dissolved Co generates in the CoCrMo particles an imbalance in the alloy, leading to the formation of intermetallic compounds rich in Mo and Cr within the solid matrix of the particle.

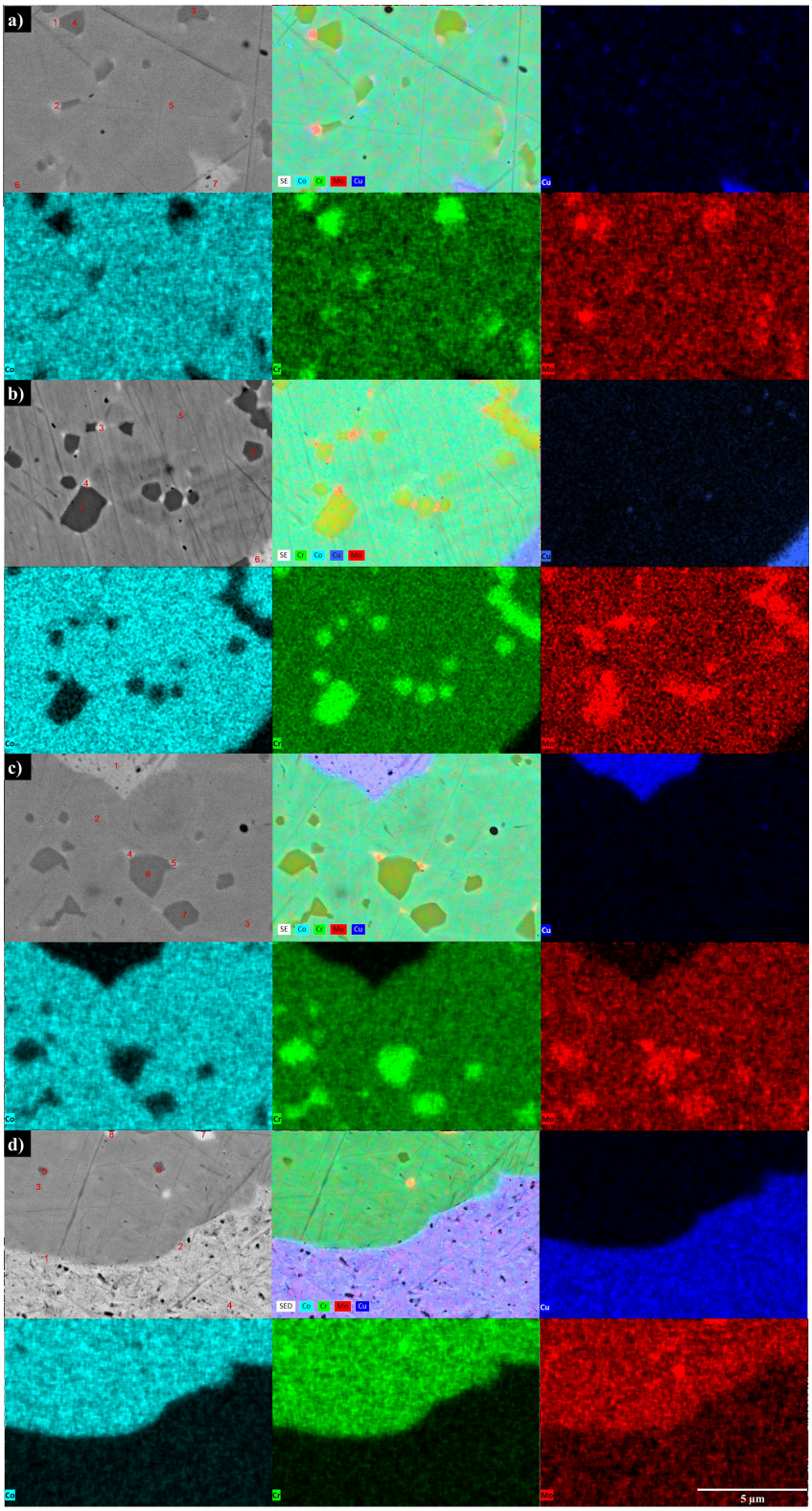
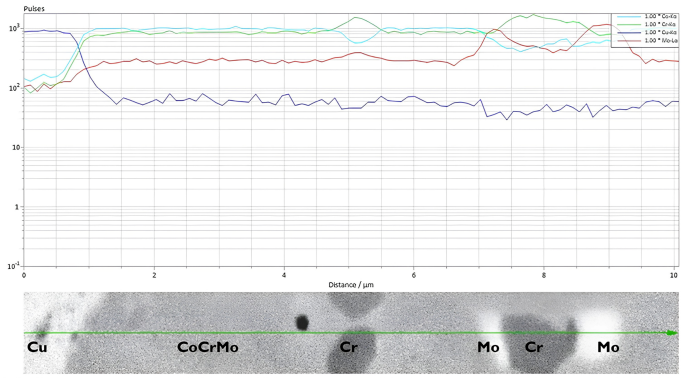


Figure 4. CoCrMo/Cu elemental mapping and EDS spot analysis for different Cu contents: 10 wt.% (**a**), 15 wt.% (**b**), 20 wt.% (**c**), and 25 wt.% (**d**).

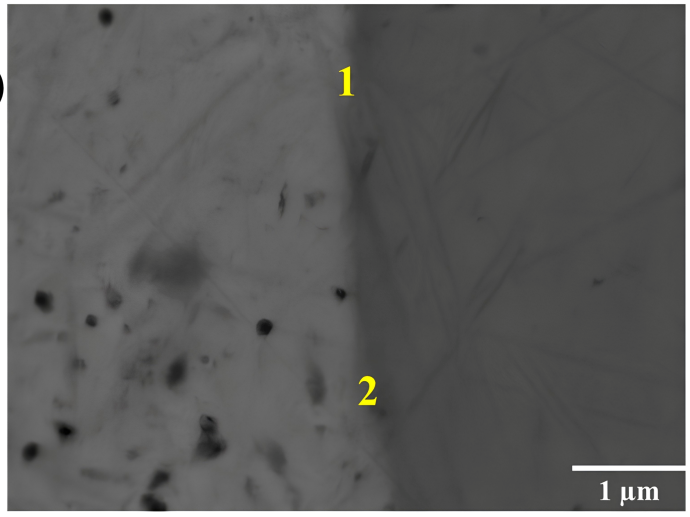
Table 2. Atomic % content from EDS analysis for the composite fabricated.

Test	Element	1	2	3	4	5	6	7	8
10Cu	Co	48.16	48.55	22.48	25.22	59.79	59.62	6.19	-
	Cr	29.25	30.06	63.73	57.78	31.22	32.17	2.54	-
	Mo	11.54	0.00	0.00	5.56	0.00	0.00	0.00	-
	Cu	10.69	18.02	13.39	11.44	8.66	7.87	91.25	-
15Cu	Co	14.53	23.62	44.06	44.35	60.82	4.92	-	-
	Cr	68.75	59.76	31.35	30.74	27.88	1.74	-	-
	Mo	6.28	5.74	13.85	13.33	3.19	0.00	-	-
	Cu	10.45	10.89	10.35	11.25	8.08	93.32	-	-
20Cu	Co	5.24	61.68	58.34	44.49	54.85	15.66	18.11	-
	Cr	1.39	29.44	32.91	28.02	33.26	71.79	69.75	-
	Mo	0.00	0.00	0.00	10.68	0.00	0.00	0.00	-
	Cu	93.36	8.60	8.44	16.56	8.26	12.08	11.71	-
25Cu	Co	7.15	9.93	66.94	3.16	57.94	60.44	64.60	61.29
	Cr	2.44	2.28	29.35	0.00	34.26	33.75	29.58	32.51
	Mo	0.00	1.08	3.71	0.00	4.29	3.15	5.76	3.73
	Cu	90.41	86.71	0.00	96.84	3.50	2.64	0.00	2.46

a)



b)



c)

E	1	2
Co	35.29	44.28
Cr	16.17	20.25
Mo	0.00	0.00
Cu	48.53	35.46

Figure 5. Line scan (**a**) and micrograph (**b**) at the CoCrMo and Cu interface of the CoCrMo25Cu compound, and atomic % content from EDS analysis (**c**) at the interface.

X-ray diffraction (XRD) was conducted on the base materials, specifically CoCrMo and copper (Cu) powders, as well as on the four composites that were manufactured (Figure 6). The diffractograms for the gamma (γ) CoCrMo showed characteristic peaks at 44.1° (111) and 75.0° (220) [37]. In contrast, Cu exhibited peaks at 43.28° (111) and 74.81° (220) [38]. The CoCrMo/xCu composites show a dual structure, comprising face-centered cubic (FCC) phases of Co and Cu, along with secondary phases resulting from the decomposition of CoCrMo. Notable among these phases were chromium (Cr)- and molybdenum (Mo)-rich precipitates, which are associated with the decomposition of the CoCrMo alloy. Additionally, CoCr intermetallics were identified at 47.149° (411) and 59° (002) [39,40], resulting from the segregation of Mo from the CoCrMo alloy. The segregation of Mo facilitated the formation of pure Mo at 39° (110) [41]. Also, the $Co_{0.52}Cu_{0.48}$ phase was detected at 50.976° (200) and 87°. This phase is unique to the composites, and its intensity increases with higher Cu content in the system. Finally, in the interface between CoCrMo and the solidified Cu, there is a non-presence of Mo, which is associated with the depletion of the CoCrMo matrix due to the formation of the intermetallic rich in Mo and the new CoCr form.

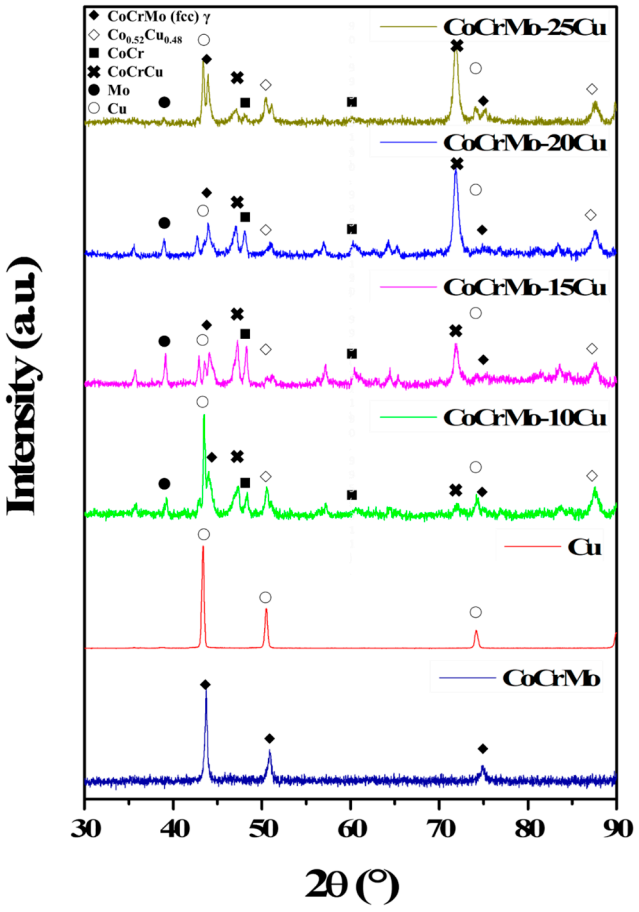


Figure 6. X-ray pattern for the four fabricated materials with different quantities of Cu, CoCrMo, and Cu powders.

The dissolution of Co by the Cu liquid at the particle surface forms a CoCrCu phase rich in Cu whose main peaks in the diffraction patterns are similar to the ones of Cu. In the sintering process, the Cu reaches the liquid phase and starts to dissolve the CoCr phase. It has been previously reported that the simulation of this ternary compound at 1100 °C is associated with a Cu liquid and the σCo phases [42]. On the other hand, Derimow and Abbaschian [43] analyzed the high entropy CoCrMo alloy and they concluded that the formation of a CoCrCu ternary compound is not thermodynamically possible due to the

enthalpy formation of the binary compounds among Co-Cr, Co-Cu and Cr-Cu. The Cu liquid dissolves the σCo phase, which is composed of Co and Cr, and when it solidifies, it traps the Co and Cr. However, it has been reported that a FCC phase exists in high entropy alloys (HEAs) between CuMn with Cr interstitials [44]; a similar phenomenon could be happening between CoCu and Cr. The CoCrCu compound was associated with the 47.1 and 71° diffraction patterns. Those phases confirmed the findings through EDS analysis by spot, line scans, and elemental mapping as discussed above.

3D images were acquired for samples with different Cu additions in order to analyze the porosity and the Cu distribution inside the composite. First, a binary (2D) analysis of the 15Cu specimen (Figure 7) was conducted to identify the phases present in the material. In (a), the fabricated composite is shown, and the Cu and porosity zones are indicated. Since the CoCrMo phases, as well as the liquid Cu, have different densities, the three phases were individually separated: the CoCrMo (b), the Cu (c), as well as the remaining pores (d). Subsequently, a cubic volume of 400 × 400 × 400 μm of the complete volume was virtually cropped for all samples to perform 3D analysis. Figure 8 shows the individual elements: the CoCrMo matrix (b and f), the melted and solidified Cu (c and g), the remaining porosity (d and h), and the volume as a whole (a and e) for the samples with 15 and 25wt.% of Cu, respectively. In both cases, the CoCrMo matrix, being in a higher proportion, is uniformly distributed. As shown in the SEM images of the 15Cu specimen, necks between spherical particles, typical of the sintering process, are observed. In the case of Cu, it is dispersed and isolated among the continuous CoCrMo matrix; as for the porosity, it is dispersed and homogeneous throughout the specimen. For the 25Cu specimen, the CoCrMo matrix exhibited greater densification; the particles grew, eliminating the necks formed between them, as the Cu is also well distributed around the CoCrMo particles, allowing for more significant densification of the specimen. In both cases, the porosity is mainly disconnected from the whole volume; pores form some agglomerate blocks isolated among them. The pore volume fractions of samples were calculated by dividing the number of voxels corresponding to the pore phase in the binary image (Figure 7d) by the total number of voxels in the image. The pore volume fraction of pores calculated from the 3D images were 20.3, 17.8, 10.5 and 6.9% for the samples with 10, 15, 20 and 25 wt.% of Cu. Those values are slightly large in comparison to the ones obtained by measuring the whole volume and mass of the samples (see Table 1). This is attributed to the resolution of the images that could overestimate the pore volume during the segmentation process to convert the gray level image into a binary one.

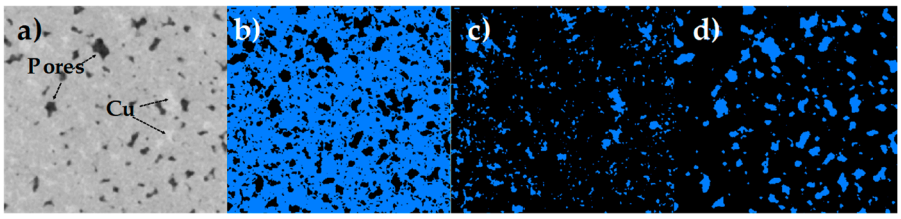


Figure 7. 2D virtual slices of the CoCrMo/15Cu composite, (**a**) initial gray-level image, and binary images obtained from the segmentation process; (**b**) CoCrMo, (**c**) Cu and (**d**) pores.

The pore size distribution was estimated from the 3D binary images by using the 3D opening technique [45], based on the characterization of the porous volume accessible to an octahedron as a structural element with increasing size, previously used by other authors [46]. The pore size distribution of samples shows a reduction in the pores as the Cu addition increases, which is due to the higher densification reached (Figure 9). The reduction in the pore sizes is quantified by measuring the median size (d_{50}) of pores. The d_{50} for the sample with 10 wt.% (19.3 μm) is twice as large as that of the one on the

composite with 25 wt.% of Cu (9.2 µm). This pore size is beneficial for some biomedical applications, as it has been pointed out that pores smaller than 10 µm could favor bone ingrowth [47]. Therefore, as can be observed, pore size and pore volume fraction could be controlled by the quantity of liquid in the system, which could allow designing for the desired porosity for biomedical applications.

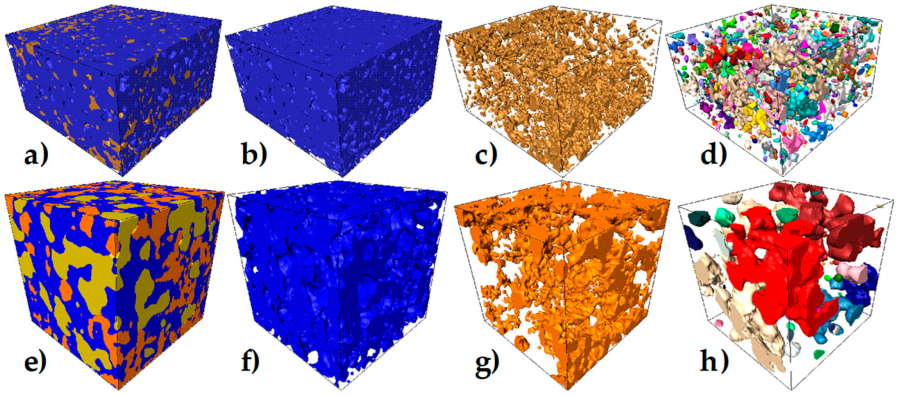


Figure 8. 3D rendering of the different phases in the composites with different Cu addition; 15 vol.% (**a**) composite, (**b**) CoCrMo, (**c**) Cu and (**d**) pores, and 25 vol.% (**e**) composite, (**f**) CoCrMo, (**g**) Cu and (**h**) pores.

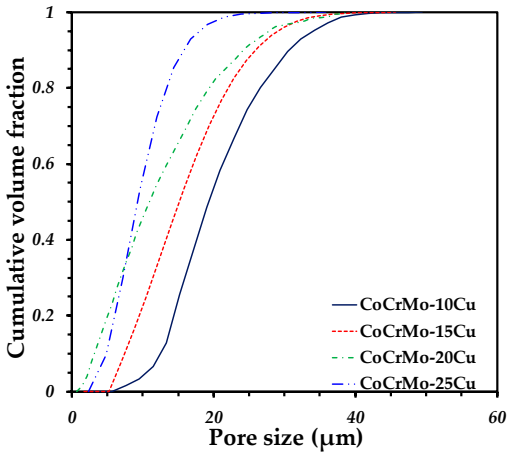


Figure 9. Pore size distribution of CoCrMo/xCu composites with different additions of Cu.

3.3. Microhardness Analysis

Microhardness tests were performed, and it was found that the microhardness increased as the Cu content increased (Figure 10), which was associated with less remaining porosity, as confirmed by SEM images and microtomography analysis. The liquid phase formed by the Cu fills the spaces, making it a denser material. However, the higher hardness values achieved for 20Cu and 25Cu are within the same range as those for CoCrMo sintered at 1200-1350 °C [3,48] and exceed those for other fabrication routes, such as SLM [1]. The incremental increase in microhardness is mainly due to the densification of samples: as was discussed, the sample with 10 wt.% of Cu had the lower densification because the liquid quantity was not enough to fill the pores. This can be noticed in the microhardness results, in which the microhardness value increases from 240 to 310 HV for a reduction in pores from 18 to 6%, for samples with 10 and 25 wt.% of Cu, respectively. However, the hardness of the composites did not show a higher reduction as soft copper was added because the formation of the intermetallic compounds, Co-Cr and Co-Mo, help to improve the hardness values. The values for the densest sample are in the range of the CoCrMo alloy; however, the CoCrMo/25Cu composite offers a lower temperature of fabrication and could offer

good antibacterial activity, thanks to the Cu addition. This could be important for bone implant applications in order to reduce the risk of implant failure by infections [49,50].

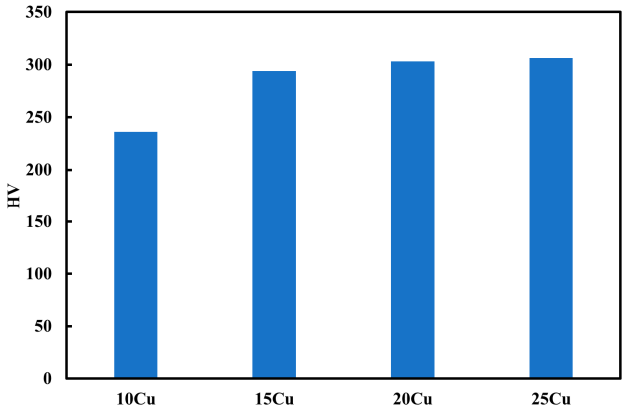


Figure 10. Microhardness (HV) of the fabricated compounds with different Cu content.

3.4. Electrochemical Analysis

The polarization curves are shown on Figure 11. It is observed that the same behavior is observed across all samples, with an equilibrium potential between −0.2 and −0.1 V vs. Ag/AgCl. The exchange current density (i_0), equilibrium potential (E_0), and corrosion rate are reported in Table 3. There are no significant differences between the samples; the corrosion rates are similar despite the variability in copper content. It is also observed that, closest to the value 0.1 V vs. $Ag/AgCl_{(sat)}$, a zone of constant current density, associated with the formation of a copper oxide film, a common product in aerated solutions, is seen [51]. However, this film provides ineffective protection due to its porosity, and the presence of chloride ions in Hank's solution can form CuCl, an intermediate product. This facilitates pore diffusion of copper ions, thereby increasing susceptibility to corrosion and pitting [52].

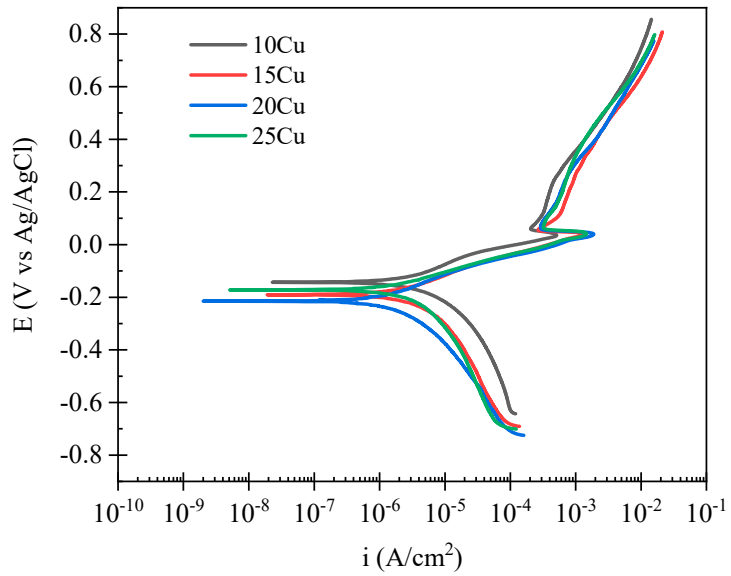


Figure 11. Polarization curve of CoCrMo with different Cu concentrations.

Results of electrochemical impedance spectroscopy (EIS) are reported. In the Nyquist plot (Figure 12b), two semicircles are observed, indicating two processes; therefore, an electrical equivalent circuit (EEC) with two constant times in parallel (Figure 12a) was used to fit the results used to describe porous systems [53]. The EEC contains a solution

resistance (R1), an outer porous oxide layer (CPE2 and R2), and an inner dense barrier oxide layer (C3 and R3) [53]. The constant phase element (CPE2) is included as a model of non-ideal capacitance arising from surface heterogeneity and roughness, in this case for the porous oxide layer [54], and comprises two parameters: Q and alpha. When the surface heterogeneity modifies the ideal capacitor behavior, the alpha is close to 1. The equivalent circuit parameters obtained from EIS are summarized in Table 4, including the chi-square (χ^2) value from the EIS data fit, which served as a goodness-of-fit parameter; lower values indicate that the fitted EIS model accurately represents the experimental data. It is observed that a higher copper concentration slightly increases both resistances, consistent with decreased porosity and the formation of a CuO_2 film.

Table 3. Corrosion parameters obtained from polarization curves.

Test	b_a (mV)	b_c (mV)	i_0 (A/cm^2)	E_0 (V vs. Ag/AgCl)	Corrosion Rate (mm/y)
10Cu	76.46	88.28	1.558×10^{-6}	−0.1408	0.0157
15Cu	65.26	82.56	1.019×10^{-6}	−0.1888	0.0103
20Cu	89.06	146.1	9.269×10^{-7}	−0.2069	0.0095
25Cu	69.14	112.7	1.077×10^{-6}	−0.1706	0.0111

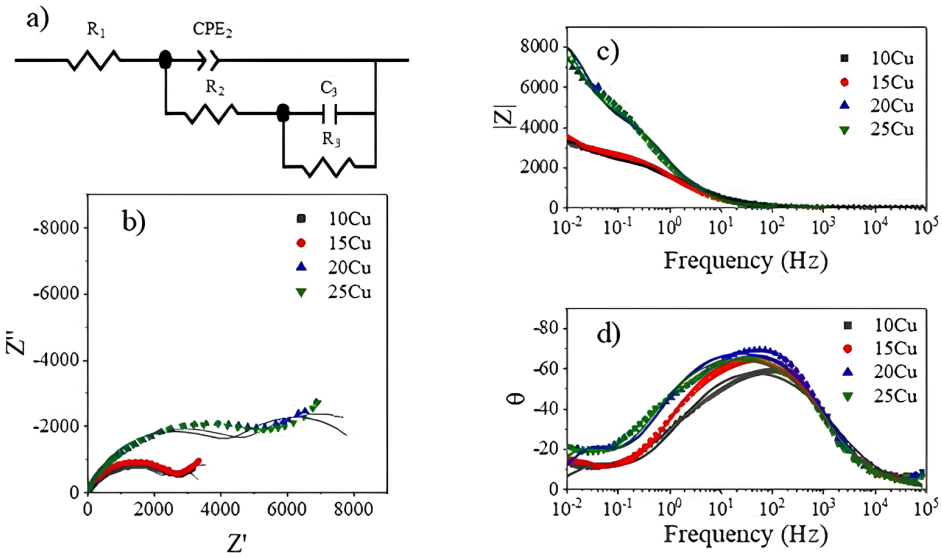


Figure 12. Electrochemical spectroscopy impedance of CoCrMo with different Cu concentrations; (**a**) electrochemical equivalent circuit, (**b**) Nyquist, (**c**) Bode module, and (**d**) Bode phase plots. The dots represent experimental results, and the continuous line represents the fitting.

Table 4. Equivalent circuit parameters calculated by fitting EIS.

Test	χ^2	R1 ($\Omega \cdot cm^2$)	Q_2 ($S \cdot s^{\alpha} \cdot cm^{-2}$)	α_2	R_2 ($\Omega \cdot cm^2$)	C_3 ($F \cdot cm^{-2}$)	R_3 ($\Omega \cdot cm^2$)
10Cu	0.0075274	15.63	8.04×10^{-5}	0.72987	2436	0.0058873	1017
15Cu	0.004035	10.68	8.55×10^{-5}	0.78425	2670	0.0089154	1543
20Cu	0.011255	10.57	7.46×10^{-5}	0.80253	4633	0.0019472	3960
25Cu	0.006667	12.73	8.63×10^{-5}	0.77116	5188	0.0029731	4153

4. Conclusions

A new CoCrMo/xCu composite was successfully developed at lower temperatures than those used to sinter CoCrMo powders. The main conclusions are as follows:

- Densification is driven by filling the pores of the Cu liquid with a partial dissolution of CoCrMo particles.
- The microstructure is formed by the CoCrMo particles, Cu, and the formation of Co-Cr and Co-Mo intermetallics due to the dissolution of cobalt at the interface with the Cu liquid.
- Reduction in pore size diameters as the densification increases was demonstrated by the 3D analysis, which can be designed to control the final porosity for different applications.
- The highest hardness values were achieved in the composites with 20% and 25% Cu, similar to CoCrMo alloys sintered at higher temperatures, which is due to the densifications reached by larger quantities of Cu liquid and the formation of the intermetallics.
- Additionally, EIS tests indicate that higher copper concentrations result in greater polarization resistance, making CoCrMo/25Cu the sample with the highest polarization resistance.

Author Contributions: L.O.: Formal analysis, Project administration, Writing—original draft. A.M.G.-C.: Investigation, Conceptualization, Writing—original draft. J.L.-R.: Writing—review and editing, Conceptualization. O.J.: Writing—review and editing, Validation. D.A.: Investigation, Software, Visualization. J.C.V.-B.: Methodology, Writing—review and editing. M.V.-P.: Methodology, Writing—review and editing. All authors have read and agreed to the published version of the manuscript.

Funding: This research was funding by the Coordinación de la Investigación Científica (CIC) of the Universiad Michoacana de San NIcolas de Hidalgo through the 2026 call for proposals, which was approved under the name of Luis Olmos.

Data Availability Statement: The data presented in this study are available on request from the corresponding author. The data are not publicly available, as they also form part of an ongoing study.

Acknowledgments: We would like to express our deep gratitude to the Instituto de Investigación en Metalurgia y Materiales/Universidad Michoacana de San Nicolás de Hidalgo for their invaluable support and collaboration in conducting this research. Their experience and dedication were essential to the success of this project.

Conflicts of Interest: The authors declare no conflicts of interest.

Abbreviations

The following abbreviations are used in this manuscript:

Cu	Copper
PM	Powder metallurgy
MMCs	Metal matrix composites
Ti	Titanium
SEM	Scanning electron microscopy
XRD	X-ray diffraction
FE-SEM	Field-emission scanning electron microscope
EIS	Electrochemical impedance spectroscopy
HV	Vickers microhardness
FCC	Face-centered cubic
Cr	Chromium
Mo	Molybdenum
HEAs	High entropy alloys
i_0	Current density
E_0	Equilibrium potential

References

1. Abdullah, A.R.; Dandang, N.A.N.; Khalil, N.Z.; Harun, W.S.W. Effect of sintering temperature on physical properties & hardness of CoCrMo alloys fabricated by metal injection moulding process. *IOP Conf. Ser. Mater. Sci. Eng.* **2017**, *257*, 012010. [CrossRef]
2. de Freitas, B.X.; Nunes, C.A.; dos Santos, C. Sintering behaviour of Co-28%Cr-6%Mo compacted blocks for dental prosthesis. *J. Mater. Res. Technol.* **2019**, *8*, 2052–2062. [CrossRef]
3. Abdull Hamid, M.H.; Mohamed Fadzil, F.S.; Selamat, M.A.; Ahmad, M.A. Sintering Effects on the Microstructure and Mechanical Properties of CoCrMo Alloy. *Adv. Mat. Res.* **2016**, *1133*, 259–263. [CrossRef]
4. Yagoob, J.A.; Abbass, M.K. Characterization of Cobalt Based CoCrMo Alloy Fabricated by Powder Metallurgy Route. In *Proceedings of the 2018 2nd International Conference for Engineering, Technology and Sciences of Al-Kitab (ICETS)*; IEEE: New York, NY, USA, 2018; pp. 1–5. [CrossRef]
5. Peaubuapuan, C.; Tunthawiroon, P.; Kanlayasiri, K.; Yuangyai, C. Effect of Si on Microstructure and Corrosion Behavior of CoCrMo Alloys. *IOP Conf. Ser. Mater. Sci. Eng.* **2018**, *361*, 012004. [CrossRef]
6. Shi, Z.; Yu, Y.; Wang, Y.; Zhang, D.; Dai, L.; Wang, M. Effect of nickel content on the processing and microstructure evolution of Co–Cr–Mo–Ni alloys. *Mater. Sci. Eng. A* **2019**, *759*, 195–202. [CrossRef]
7. Jamal Al-Deen, H.H.J.; Alhusseini, Z.A.K. Influence of zirconia addition on corrosion behavior of biomedical COCrMo Alloys(F75). *AIP Conf. Proc.* **2023**, *2830*, 030039. [CrossRef]
8. Peter, I.; Rosso, M. Study of Ti-Enriched CoCrMo Alloy for Dental Application. *IEEE Access* **2015**, *3*, 73–80. [CrossRef]
9. Cui, G.; Liu, Y.; Li, S.; Liu, H.; Gao, G.; Kou, Z. Nano-TiO_2 reinforced CoCr matrix wear resistant composites and high-temperature tribological behaviors under unlubricated condition. *Sci. Rep.* **2020**, *10*, 6816. [CrossRef]
10. Zhang, L.; Liu, W.; Cao, Y.; Sun, H.; Xie, Q.; Lai, J.; Bai, P. Effect of Co-Coated Al_2O_3 Composite Powders on LPBF-Manufactured CoCrMo Alloy. *Metals* **2023**, *13*, 310. [CrossRef]
11. Bandyopadhyay, A.; Shivaram, A.; Isik, M.; Avila, J.D.; Dernell, W.S.; Bose, S. Additively manufactured calcium phosphate reinforced CoCrMo alloy: Bio-tribological and biocompatibility evaluation for load-bearing implants. *Addit. Manuf.* **2019**, *28*, 312–324. [CrossRef] [PubMed]
12. Onderka, F.; Volodarskaja, A.; Kadlec, J.; Dobrocký, D.; Klanica, O. Electrochemical Deposition of Hydroxyapatite Coatings on CoCrMo Alloy. *ECS Trans.* **2014**, *63*, 277–289. [CrossRef]
13. Wang, P.; Yuan, Y.; Xu, K.; Zhong, H.; Yang, Y.; Jin, S.; Yang, K.; Qi, X. Biological applications of copper-containing materials. *Bioact. Mater.* **2021**, *6*, 916–927. [CrossRef]
14. Wang, R.; Qin, G.; Zhang, E. Effect of Cu on Martensite Transformation of CoCrMo alloy for biomedical application. *J. Mater. Sci. Technol.* **2020**, *52*, 127–135. [CrossRef]
15. Shen, Q.; Qi, Y.; Kong, Y.; Bao, H.; Wang, Y.; Dong, A.; Wu, H.; Xu, Y. Advances in Copper-Based Biomaterials With Antibacterial and Osteogenic Properties for Bone Tissue Engineering. *Front. Bioeng. Biotechnol.* **2022**, *9*, 795425. [CrossRef]
16. Wu, S.; Wang, Q.; Li, Y.; Liu, B.; Miao, Y. Recent Advances in the Biomedical Applications of Copper Nanomaterial-Mediated Cuproptosis. *Adv. Nanobiomed. Res.* **2024**, *4*, 2400018. [CrossRef]
17. Wei, Q.; Pan, Y.; Zhang, Z.; Yan, S.; Li, Z. Copper-based nanomaterials for biomedical applications. *Chem. Eng. J.* **2024**, *483*, 149040. [CrossRef]
18. Chen, X.; Bao, R.; Yi, J.; Fang, D.; Tao, J.; Li, F. Enhancing mechanical properties of pure copper-based materials with Cr_xO_y nanoparticles and CNT hybrid reinforcement. *J. Mater. Sci.* **2021**, *56*, 3062–3077. [CrossRef]
19. de Oro Calderon, R.; Gierl-Mayer, C.; Danninger, H. Fundamentals of Sintering: Liquid Phase Sintering. In *Encyclopedia of Materials: Metals and Alloys*; Elsevier: Amsterdam, The Netherlands, 2022; pp. 481–492. [CrossRef]
20. Huang, C.; Yuan, N.; He, X.; Wang, C. Ceramsite made from drinking water treatment residue for water treatment: A critical review in association with typical ceramsite making. *J. Environ. Manag.* **2023**, *328*, 117000. [CrossRef]
21. Korda, A.A.; Munawaroh, S.; Basuki, E.A. The Antimicrobial Activity and Characterization of the Cast Titanium Copper Alloys with Variations of Copper Content. *IOP Conf. Ser. Mater. Sci. Eng.* **2019**, *547*, 012002. [CrossRef]
22. Zhuang, Y.; Ren, L.; Zhang, S.; Wei, X.; Yang, K.; Dai, K. Antibacterial effect of a copper-containing titanium alloy against implant-associated infection induced by methicillin-resistant Staphylococcus aureus. *Acta Biomater.* **2021**, *119*, 472–484. [CrossRef]
23. Ma, Z.; Ren, L.; Liu, R.; Yang, K.; Zhang, Y.; Liao, Z.; Liu, W.; Qi, M.; Misra, R.D.K. Effect of Heat Treatment on Cu Distribution, Antibacterial Performance and Cytotoxicity of Ti–6Al–4V–5Cu Alloy. *J. Mater. Sci. Technol.* **2015**, *31*, 723–732. [CrossRef]
24. Yamanaka, K.; Mori, M.; Yoshida, K.; Onuki, Y.; Sato, S.; Chiba, A. Surface evolution and corrosion behaviour of Cu-doped carbide-reinforced martensitic steels in a sulfuric acid solution. *npj Mater. Degrad.* **2021**, *5*, 43. [CrossRef]
25. Wang, S.; Yang, C.; Shen, M.; Yang, K. Effect of aging on antibacterial performance of Cu-bearing martensitic stainless steel. *Mater. Technol.* **2014**, *29*, 257–261. [CrossRef]
26. Chai, H.; Guo, L.; Wang, X.; Fu, Y.; Guan, J.; Tan, L.; Ren, L.; Yang, K. Antibacterial effect of 317L stainless steel contained copper in prevention of implant-related infection in vitro and in vivo. *J. Mater. Sci. Mater. Med.* **2011**, *22*, 2525–2535. [CrossRef]

27. Xi, T.; Shahzad, M.B.; Xu, D.; Sun, Z.; Zhao, J.; Yang, C.; Qi, M.; Yang, K. Effect of copper addition on mechanical properties, corrosion resistance and antibacterial property of 316L stainless steel. *Mater. Sci. Eng. C* **2017**, *71*, 1079–1085. [CrossRef]
28. Li, W.; Wang, X.; Liu, C.; Qin, G.; Zhang, E. Effect of heat treatment on the bio-corrosion properties and wear resistance of antibacterial Co-29Cr-6Mo-xCu alloys. *J. Mater. Sci. Mater. Med.* **2019**, *30*, 112. [CrossRef]
29. Uzun, M.; Çetin, M.S. Investigation of characteristics of Cu based, Co-CrC reinforced composites produced by powder metallurgy method. *Adv. Powder Technol.* **2021**, *32*, 1992–2003. [CrossRef]
30. Elder, S.P.; Munitz, A.; Abbaschian, G.J. Metastable Liquid Immiscibility in Fe-Cu and Co-Cu Alloys. *Mater. Sci. Forum* **1991**, *50*, 137–150. [CrossRef]
31. Liu, Y.; Tandon, R.; German, R.M. Modeling of Supersolidus Liquid Phase Sintering: I. Capillary Force. *Metall. Mater. Trans. A* **1995**, *26*, 2415–2422. [CrossRef]
32. Liu, Y.; Tandon, R.; German, R.M. Modeling of Supersolidus Liquid Phase Sintering: II. Densification. *Metall. Mater. Trans. A* **1995**, *26*, 2423–2430. [CrossRef]
33. Cao, C.D.; Görler, G.P.; Herlach, D.M.; Wei, B. Liquid–Liquid Phase Separation in Undercooled Co–Cu Alloys. *Mater. Sci. Eng. A* **2002**, *325*, 503–510. [CrossRef]
34. Munitz, A.; Elder-Randall, S.P.; Abbaschian, R. Supercooling Effects in Cu-10 Wt Pct Co Alloys Solidified at Different Cooling Rates. *Metall. Trans. A* **1992**, *23*, 1817–1827. [CrossRef]
35. Munitz, A.; Abbaschian, R. Microstructure of Cu-Co Alloys Solidified at Various Supercoolings. *Metall. Mater. Trans. A* **1996**, *27*, 4049–4059. [CrossRef]
36. Egry, I.; Ratke, L.; Kolbe, M.; Chatain, D.; Curiotto, S.; Battezzati, L.; Johnson, E.; Pryds, N. Interfacial properties of immiscible Co–Cu alloys. *J. Mater. Sci.* **2010**, *45*, 1979–1985. [CrossRef]
37. Ahmad, T. Ascorbic acid assisted synthesis, characterization and catalytic application of copper nanoparticles. *Mater. Sci. Eng. Int. J.* **2018**, *2*, 90–94. [CrossRef]
38. Welles, T.S.; Ahn, J. Driving electrochemical corrosion of implanted CoCrMo metal via oscillatory electric fields without mechanical wear. *Sci. Rep.* **2021**, *11*, 22366. [CrossRef]
39. Majerič, D.; Lazić, V.; Majerič, P.; Marković, A.; Rudolf, R. Investigation of CoCr Dental Alloy: Example from a Casting Workflow Standpoint. *Crystals* **2021**, *11*, 849. [CrossRef]
40. Zhao, H.; Xie, J.; Mao, A.; Wang, A.; Chen, Y.; Liang, T.; Ma, D. Effects of Heating Mode and Temperature on the Microstructures, Electrical and Optical Properties of Molybdenum Thin Films. *Materials* **2018**, *11*, 1634. [CrossRef]
41. Jia, X.; Lin, Z.; Yang, T.C.-J.; Puthen-Veettil, B.; Wu, L.; Conibeer, G.; Perez-Wurfl, I. Post-Sputtering Heat Treatments of Molybdenum on Silicon Wafer. *Appl. Sci.* **2018**, *8*, 1692. [CrossRef]
42. Liu, X.J.; Jiang, Z.P.; Wang, C.P.; Ishida, K. Experimental determination and thermodynamic calculation of the phase equilibria in the Cu–Cr–Nb and Cu–Cr–Co systems. *J. Alloys Compd.* **2009**, *478*, 287–296. [CrossRef]
43. Derimow, N.; Abbaschian, R. Solidification Microstructures and Calculated Mixing Enthalpies in CoCrCu Containing Alloys. *Mater. Today Commun.* **2018**, *15*, 1–10. [CrossRef]
44. He, W.; Zeng, C.; Yang, W.; Chen, W.; Ai, Y. Impact of different Cr contents on microstructural evolution and mechanical behaviour of CoCrxCuFeMnNiV high-entropy alloys. *J. Mater. Res. Technol.* **2022**, *21*, 4577–4590. [CrossRef]
45. Young, I.T. Image Analysis and Mathematical Morphology, by J. Serra. Academic Press, London, 1982, Xviii + 610 p. $90.00. *Cytometry* **1983**, *4*, 184–185. [CrossRef]
46. Olmos, L.; Takahashi, T.; Bouvard, D.; Martin, C.L.; Salvo, L.; Bellet, D.; Di Michiel, M. Analysing the Sintering of Heterogeneous Powder Structures by in Situ Microtomography. *Philos. Mag.* **2009**, *89*, 2949–2965. [CrossRef]
47. Braem, A.; Chaudhari, A.; Vivan Cardoso, M.; Schrooten, J.; Duyck, J.; Vleugels, J. Peri- and Intra-Implant Bone Response to Microporous Ti Coatings with Surface Modification. *Acta Biomater.* **2014**, *10*, 986–995. [CrossRef]
48. Garcia-Carrillo, A.M.; Lemus-Ruiz, J.; Olmos, L. Sintering Analysis of CoCrMo Powders by in-Situ Dilatometry. *Mater. Res.* **2024**, *27*, e20240286. [CrossRef]
49. Celles, C.A.S.; dos Reis, A.C. Effect of Copper Incorporated into Titanium (Cp-Ti) and Its Alloys (Ti-6Al-4V) and Its Promising Antibacterial Effect: A Systematic Review. *Dent. Rev.* **2025**, *5*, 100156. [CrossRef]
50. Yang, S.; Pan, J.; Zhang, H.; Ling, H. Effect of Ag and Cu Additions on Antibacterial Performance of Fe-Based Amorphous Alloys. *BioMetals* **2026**, *39*, 259–267. [CrossRef]
51. Acciari, H.A.; Guastaldi, A.C.; Brett, C.M.A. Corrosion of the component phases presents in high copper dental amalgams. Application of electrochemical impedance spectroscopy and electrochemical noise analysis. *Corros. Sci.* **2005**, *47*, 635–647. [CrossRef]
52. Benzarti, Z.; Arrousse, N.; Serra, R.; Cruz, S.; Bastos, A.; Tedim, J.; Salgueiro, R.; Cavaleiro, A.; Carvalho, S. Copper corrosion mechanisms, influencing factors, and mitigation strategies for water circuits of heat exchangers: Critical review and current advances. *Corros. Rev.* **2025**, *43*, 429–455. [CrossRef]

53. Alves, A.C.; Wenger, F.; Ponthiaux, P.; Celis, J.-P.; Pinto, A.M.; Rocha, L.A.; Fernandes, J.C.S. Corrosion mechanisms in titanium oxide-based films produced by anodic treatment. *Electrochim. Acta* **2017**, *234*, 16–27. [CrossRef]
54. Cassar, M.B.; Karl, A.; Buhagiar, J. EIS of carburised CoCrMo: Evolution of parameters characterising the metal-electrolyte interface. *Surf. Coat. Technol.* **2016**, *292*, 90–98. [CrossRef]

Disclaimer/Publisher's Note: The statements, opinions and data contained in all publications are solely those of the individual author(s) and contributor(s) and not of MDPI and/or the editor(s). MDPI and/or the editor(s) disclaim responsibility for any injury to people or property resulting from any ideas, methods, instructions or products referred to in the content.